Model-based thermal runaway prediction of lithium-ion batteries from kinetics analysis of cell components

Dongsheng Ren[a], Xiang Liu[a], Xuning Feng[a,b], Languang Lu[a], Minggao Ouyang[a,*], Jianqiu Li[a], Xiangming He[a,b]

[a] State Key Laboratory of Automotive Safety and Energy, Tsinghua University, Beijing 100084, China
[b] Institute of Nuclear and New Energy Technology, Tsinghua University, Beijing 100084, China

HIGHLIGHTS

- The battery TR mechanism is characterized by DSC tests on cell components.
- Six exothermic reactions are determined as the dominant heat sources.
- The kinetics parameters of each exothermic reactions are identified.
- A battery TR model is established by coupling all the exothermic reactions.
- The model predictions fit well with the variant TR tests results.

ARTICLE INFO

ABSTRACT

Thermal runaway (TR) is a major safety concern in lithium-ion batteries. Model-based TR prediction is critically needed to optimize safety designs of cells. This paper presents a novel scheme for developing reliable battery TR model from kinetics analysis of cell components. First, differential scanning calorimetry (DSC) tests on the individual cell components and their mixtures are conducted to reveal the TR mechanism and characterize the exothermic reactions, of which the major six (such as the decomposition of solid electrolyte interface (SEI) film) are determined as the dominant heat sources. The kinetics parameters of each exothermic reactions are identified from the DSC tests results at variant heating rates using Kissinger's method and nonlinear fitting method. A predictive battery TR model is established by superimposing the chemical kinetics equations of the six exothermic reactions. The model fits well with the adiabatic TR test results and the oven tests results of a 24 Ah lithium-ion battery, indicating that the model can well reflect the battery TR mechanism and be trusted to predict battery safety performance without assembling a real battery.

1. Introduction

Lithium-ion batteries, with high energy density and extended cycle life, are the most widely used power sources for electric vehicles (EVs) [1–5]. Recent years, battery manufacturers are developing new materials to improve the energy density of lithium-ion batteries. For example, to develop the lithium-ion battery with a high energy density of 300 Wh kg^{-1}, the cathode materials may change from Li(Ni$_{1/3}$Co$_{1/3}$Mn$_{1/3}$)O$_2$ to Ni-rich Li(Ni$_x$Co$_y$Mn$_z$)O$_2$ cathode like Li(Ni$_{0.8}$Co$_{0.1}$Mn$_{0.1}$)O$_2$ or Li-rich manganese oxide etc., whereas the anode materials are changing from graphite to Si-C composite anode [3,4]. However, electrode materials with higher energy density have lower thermal stability, leading to potential safety problems, such as thermal runaway

(TR) [6–10]. As a result, more attention should be paid to the thermal stability of the high energy density electrode materials, when applied in mass-produced large format lithium-ion batteries.

To evaluate the safety of the lithium-ion battery, manufacturers may need to produce a certain number of batteries and perform a series of safety tests [11]. Several "build and break" cycles are essential for developing a battery with a new chemistry design. However, "trial-and-error" tests are laboring work with low efficiency and provide limit information for battery safety improvement. Therefore, mathematical modeling should be developed to predict battery safety behaviors, which can help to reduce the number of "trial-and-error" tests and optimize battery designs.

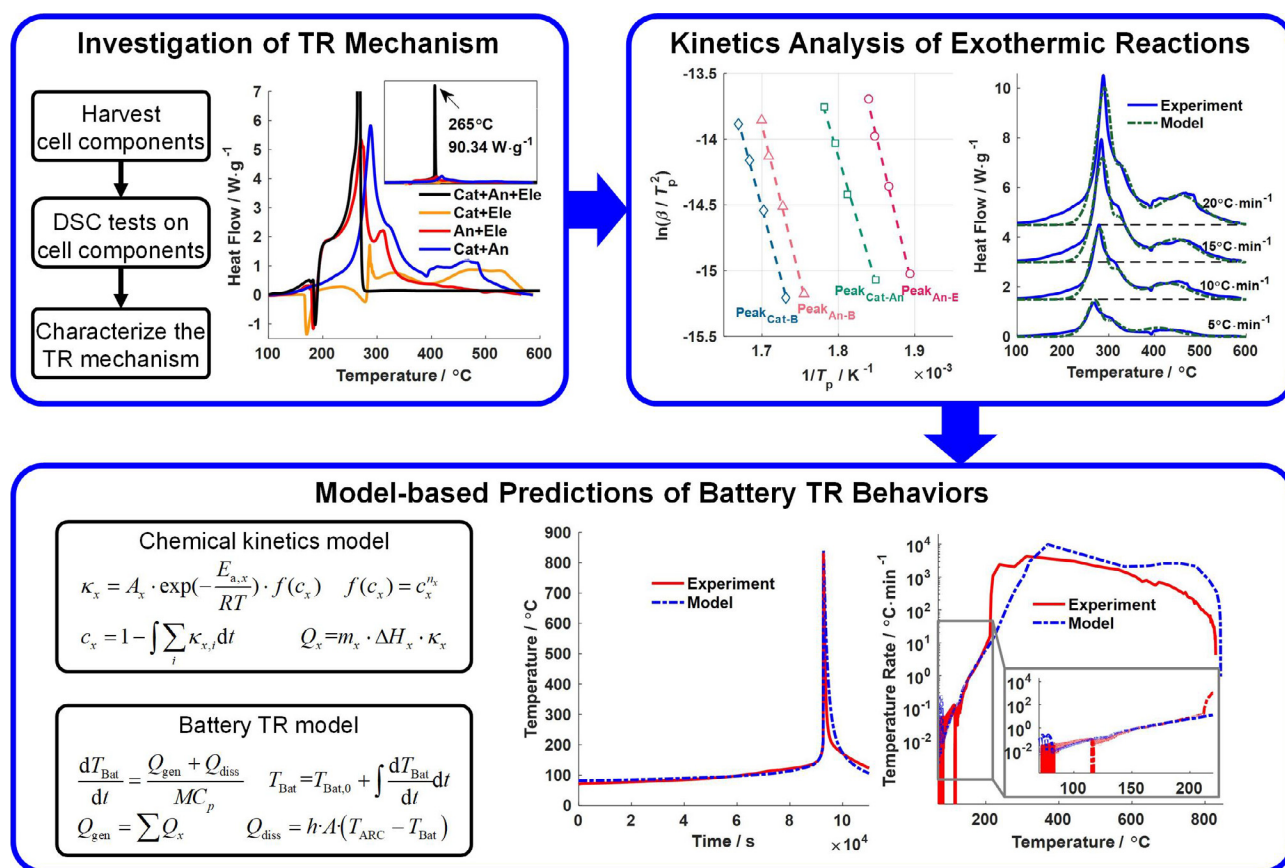Several investigations on the TR mechanism of lithium-ion batteries

Fig. 1. Model-based TR prediction of lithium-ion batteries from kinetics analysis of cell components—an overview of this paper.

were conducted from both the component level and cell level, using differential scanning calorimetry (DSC) and accelerating rate calorimeter (ARC) [6,7,12–15]. Several exothermic reactions have contributions to the battery TR features. When the temperature rises up to 70–90 °C, the battery starts self-heating due to the decomposition of solid electrolyte interface (SEI) film [14–17], followed by the reaction between anode active material and electrolyte [18,19], and the reaction between anode active material and binder [20,21] at elevated temperature. The cathode active material also decomposes and generates oxygen as the battery temperature goes higher [22–25]. The released oxygen can oxidize the electrolyte [22,26,27] or even react with the anode active material [28,29], bringing the battery temperature to a higher value. Combustion of the flammable gases, such as the gasified solvents and the gases (such as H_2, CO, CH_4, C_2H_6, C_2H_4) released from the chemical reactions, would happen at high temperature if ignition source exists, resulting in fire and explosion [30–32]. The combustion always occurs outside the battery and may cause significant damage on the accessories in the battery module [31,33,34].

Chemical kinetics models based on Arrhenius equations, with the kinetics parameters (pre-frequency factor, activation energy, mechanism function and reaction enthalpy) determined from ARC or DSC tests, have been developed to reveal the reaction mechanisms and predict the thermal stability of cell components. Dahn et al. has calculated the kinetics parameters of several exothermic reactions from the Arrhenius plots in the ARC tests, and established models for the SEI film decomposition reaction [16], the reaction between lithiated graphite and electrolyte [17], and the Li_xCO_2 decomposition reaction [35–37]. The kinetics parameters of the decomposition reactions of

several cathode materials, such as Li_xCO_2 and $Li_x(Ni_{1/3}Co_{1/3}Mn_{1/3})O_2$, have been investigated based on DSC tests results using Kissinger's method and Ozawa's method [24,38–41]. For anode materials, Chen et al. [19,42] has calculated the activation energy of the SEI film decomposition reaction in four types of graphite anodes from DSC tests results. Ping et al. [26,43] has proposed a deconvolution method to separate the overlapped exothermic peaks in the C80 tests results and then analyzed the kinetics parameters of each deconvoluted reaction. Furthermore, Spotnitz et al. [6] has summarized the reaction kinetics of variant cathode and anode materials. However, those existing thermal kinetics studies of cell components mainly focused on one or two specific exothermic reactions, while battery TR predictions need to establish chemical kinetics models for all the exothermic reactions. Thus, further investigations are required to characterize all the exothermic reactions during the TR process and identify their kinetics parameters.

TR models have been established based on the kinetics studies of cell components to predict the battery safety behaviors. Dahn et al. [44] has developed a battery TR model based on the kinetics models of three exothermic reactions. Dahn's model could predict the onset of battery TR well when comparing to the oven tests, but failed in the prediction of the maximum temperature, since not all the exothermic reactions were included in the model. Kim et al. [45] has established a three-dimensional thermal abuse model to study the effects of size and local hot spot on battery TR behaviors. Based on Dahn's model and Kim's model, some researchers have investigated the influences of heat release conditions [46–48], cell physical configurations [48,49], and the venting behaviors [50,51] on battery TR behaviors. Moreover, researchers have extended the battery TR model to investigate the

internal short circuit [52–54], nail penetration [55,56] and overcharge [57] behaviors of lithium-ion batteries and the TR propagation behaviors of battery modules [31,46,55]. However, most of the presented modeling works were based on Dahn's model and Kim's model with the kinetics parameters directly derived from [6,44,45] or fitted to match the experiment results, regardless of the differences in battery chemistry. That reduces the accuracy of battery TR models when applied to quantitatively predict battery safety behaviors and optimize battery chemistry designs.

Therefore, this paper aims to propose a novel approach to develop a predictive battery TR model based on kinetics analysis of all the exothermic reactions. Fig. 1 presents an overview of this paper. The battery TR mechanism is firstly investigated using DSC, and all the exothermic reactions are characterized by comparing the DSC test results of cell components harvested from a fully-charged battery. Kinetics parameters of each exothermic reaction are identified from the DSC tests results at variant heating rates using Kissinger's method and nonlinear fitting method. A battery TR model is then developed by coupling the chemical kinetics models of the six exothermic reactions. The model predictions are compared to adiabatic TR test results and oven tests results of a 24 Ah lithium-ion battery and show to be in good agreement. Thus, the model can be applied to predict the battery TR behaviors accurately without producing a test batch of cells, and then help to save the cost for safety evaluation of lithium-ion batteries.

2. Experiments

2.1. DSC tests on cell components

Prior to DSC tests, a 24 Ah Li(Ni$_{1/3}$Co$_{1/3}$Mn$_{1/3}$)O$_2$/graphite battery was fully charged to 4.2 V by the constant current(1/3C)-constant voltage (1/20C cut-off current) charging profile at 25 °C. The Li(Ni$_{1/3}$Co$_{1/3}$Mn$_{1/3}$)O$_2$ cathodes and graphite anodes were harvested from the fully-charged battery, which was dismantled in an argon-filled glove box. The electrodes were rinsed with dimethyl carbonate (DMC) for 2 h and dried in the glove box for 2 more hours to eliminate the residual lithium salt (LiPF$_6$). Then, the electrode materials were scratched off from the current collectors and grinded slightly for subsequent DSC tests. Please note that the electrode materials can also be obtained from battery manufacturers directly without assembling a real battery.

DSC tests were conducted to investigate the thermal stability of cell components using a DSC 214 Polyma (NETZSCH, Germany). As listed in Table 1, seven kinds of samples composed of individual cell components or their mixtures were prepared for DSC tests to characterize the exothermic reactions and decouple their contributions to the total heat generation of the battery. The electrolyte used for DSC tests was 1 M LiPF$_6$ in dimethyl carbonate (DMC): ethyl methyl carbonate (EMC):

Table 1
Samples for DSC tests.

Sample no.	Composition	Mass	Heating rates
1	Cathode + Anode + Electrolyte (Cat + An + Ele)	6 mg + 3.4 mg + 3 mg	20 °C min^{-1}
2	Cathode + Electrolyte (Cat + Ele)	6 mg + 3 mg	20 °C min^{-1}
3	Anode + Electrolyte (An + Ele)	3.4 mg + 3 mg	5, 10, 15, 20 °C min^{-1}
4	Cathode + Anode (Cat + An)	6 mg + 3.4 mg	5, 10, 15, 20 °C min^{-1}
5	Cathode (Cat)	6 mg	20 °C min^{-1}
6	Anode (An)	6 mg	20 °C min^{-1}
7	Electrolyte (Ele)	3 mg	20 °C min^{-1}

ethylene carbonate (EC) (1:1:1 in volume), the same as that used in the 24 Ah battery. The mass ratios between the cathode material, anode material and electrolyte were determined according to the battery specification. The test samples were sealed into standard aluminum crucibles (30 μL, concavus crucible with lid, NETZSCH, Germany) in the argon-filled glove box. DSC tests were firstly conducted at a heating rate of 20 °C min^{-1} from room temperature to 600 °C, in nitrogen atmosphere with the gas flow rate set as 40 mL min^{-1}. For further kinetics analysis, DSC tests at four heating rates (5 °C min^{-1}, 10 °C min^{-1}, 15 °C min^{-1} and 20 °C min^{-1}) were performed on sample Anode + Electrolyte (An + Ele) and sample Cathode + Anode (Cat + An), which turn out to be the two dominant exothermic reaction pairs during the TR process.

2.2. TR tests using extended volume accelerating rate calorimeter (EV-ARC)

TR tests were carried out on the fully charged 24 Ah lithium-ion batteries in an EV-ARC manufactured by Thermal Hazard Technology (THT). As shown in Fig. 2, two batteries connected in parallel were utilized for TR tests. K type thermocouple (TC1) provided by Pico Technology was inserted between the two batteries to monitor the internal temperature. The N type thermocouple of the EV-ARC (main TC) was attached on the surface of one battery. The two batteries were wrapped by high temperature insulation Kapton tape to keep compact contact during TR tests. The internal temperature recorded by the TC1 was used to characterize the battery TR behaviors and model validation in the following sections.

Two kinds of TR tests were conducted on the 24 Ah lithium-ion batteries, including adiabatic TR test and oven tests, as summarized in Table 2.

For the adiabatic TR test, the EV-ARC were operated under the Heat-Wait-Seek mode to search possible exothermic behaviors of the tested batteries. The test settings are listed in Table 2. If the temperature rate of the batteries exceeds 0.01 °C min^{-1}, the ARC system would go into the exotherm mode to track the temperature rise and maintain the adiabatic condition. In the exotherm mode, the tested batteries were self-heated up by the exothermic reactions and finally ran into thermal runaway.

For the oven tests, the batteries were initially heated up to the target temperature (i.e. 130 °C and 150 °C) at a heating rate of around 4 °C min^{-1}, then rested for 30 min to reach thermal equilibrium. The EV-ARC was set to cool mode manually after the 30 min rest period. The batteries would be cooled down if the exothermic reactions can be terminated during the cool mode or run into thermal runaway when the exothermic reactions continued.

3. Results and discussions

3.1. Investigation of TR mechanism based on DSC tests

The DSC tests results of the samples listed in Table 1 are compared in Fig. 3, and the total heat generations are collected in Table 3. The heat flow values and the heat generations presented in Fig. 3 and Table 3 have been normalized with the weight of the mixture of cathode and anode materials (9.4 mg) for comparison.

As shown in Fig. 3(a), sample Cathode + Anode + Electrolyte (Cat + An + Ele) with all the cell components mixed together showed exothermic behavior when the temperature exceeded 100 °C and exhibited a drastic exothermic peak at 265 °C, with all the materials reacting violently in a short time and the heat flow reaching 90.34 W g^{-1}. The heat generation of sample Cat + An + Ele was 1550.0 J g^{-1} in total. An endothermic peak can be found at around 170 °C, resulting from the

Fig. 2. Experimental settings of the TR tests using EV-ARC.

Table 2
TR tests using EV-ARC.

No.	Test	Test settings
1	Adiabatic TR test	Heat-Wait-Seek mode: Start temperature is 40 °C, followed by a 30 min wait period and a 20 min seek period, temperature step is 5 °C and temperature rate sensitivity is set as 0.01 °C min^{-1}
2	130 °C oven test	Heat to 130 °C, wait for 30 min and cool down
3	150 °C oven test	Heat to 150 °C, wait for 30 min and cool down

Table 3
Heat generation of the tested samples at the heating rate of 20 °C min^{-1}.

Sample	Heat generation/J g^{-1}
Cat + An + Ele	1550.0
Cat + Ele	428.1
An + Ele	940.4
Cat + An	1446.7
Cat	403.6
An	306.5
Ele	−108.6

vaporization of DMC and EMC [58] and venting of the sealed crucible. Same endothermic peaks were also observed in other samples containing electrolyte, as showed in Fig. 3(a) and (b).

For sample Cat + Ele, no exothermic behavior was observed until 250 °C, and only small amount of heat was released from 250 °C to 600 °C (428.1 J g^{-1}), nearly the same as the heat generation of sample
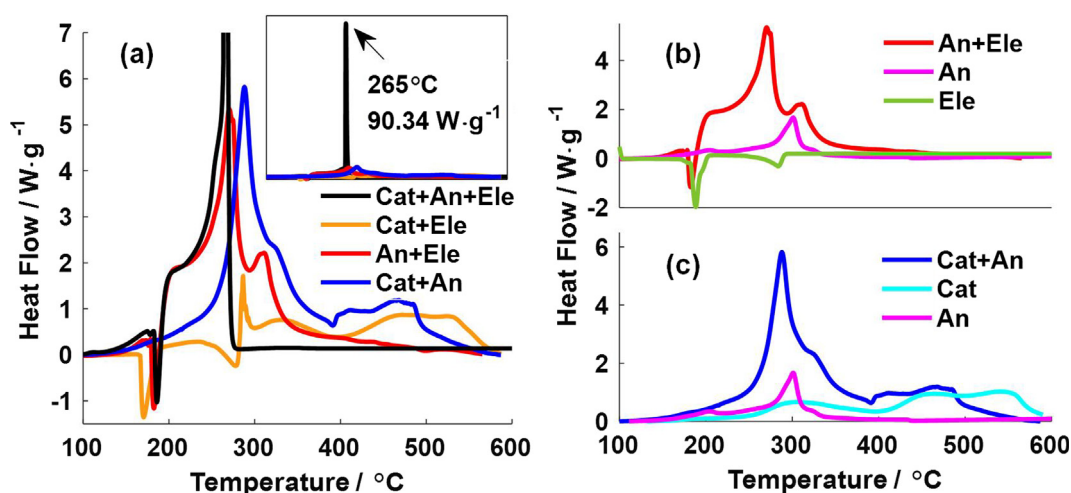

Fig. 3. Comparison of DSC tests results at the heating rate of 20 °C min^{-1}. (a) DSC profiles of the tested samples with cell components mixed together; (b) investigation of exothermic reactions between anode and electrolyte; (c) investigation of exothermic reactions between cathode and anode.

Ca(403.6 J g^{-1}). That indicated that the heat generation of sample Cat + Ele was dominated by the self-decomposition of cathode active material, while the reaction between cathode active material and electrolyte produced limited heat, mainly due to the vaporization of the solvents (the boiling temperatures of DMC, EMC and EC are 91 °C, 110 °C and 248 °C, respectively [58]) before the release of oxygen from the cathode active material at around 250 °C.

The exothermic reactions between anode and electrolyte and those between cathode and anode turned out to be the dominated heat sources during battery TR process, as sample An + Ele and sample Cat + An exhibited significant heat generation (926.0 J g^{-1} and 1446.8 J g^{-1}, respectively). Sample An + Ele showed similar exothermic behavior as sample Cat + An + Ele before 250 °C, as their heat flow profiles almost overlapped before 250 °C (as shown in Fig. 3(a)). Therefore, the battery heat generation before 250 °C was dominated by the reactions on the anode/electrolyte interface, such as the decomposition of SEI film [14–17], and the reaction between anode active material and electrolyte [18,19]. The reactions in sample Cat + An began to contribute to the total battery heat generation after the temperature reached 250 °C, as showed in Fig. 3(a).

Detailed investigation of exothermic behaviors in sample An + Ele are presented in Fig. 3(b). As shown in Fig. 3(b), three exothermic peaks can be found in the DSC profile of sample An + Ele, at around 200 °C, 270 °C and 315 °C, respectively. The first exothermic peak at 200 °C was attributed to the decomposition of SEI film (both original and re-generated SEI film) [14–17], and the second peak resulted from the reaction between anode active material and electrolyte [18,19], while the third peak represented the reaction between anode active material and binder [20,21], which can also be observed in the DSC profile of sample An.

The heat generation of sample Cat + An started at around 250 °C, consistent with the decomposition of cathode active material, as shown in Fig. 3(c). Oxygen was released from the decomposition of cathode active material, as shown in Fig. B1. The oxygen will react with the anode active material at elevated temperature [28,29], leading to a distinct exothermic peak at around 290 °C in the DSC profile of sample Cat + An. The released oxygen can also react with the binder [59], and showed exothermic peak at around 320 °C. The total temperature range of the reaction between released oxygen and anode active material as well as binder was approximately between 250 and 400 °C, nearly the same as the temperature range of the first decomposition reaction in sample Cat, as shown in Fig. 3(c). A broad exothermic peak was observed between 400 °C and 600 °C in the DSC profile of sample Cat + An, mainly due to the subsequent decomposition reaction of cathode active material, as sample Cat exhibited similar exothermic peak.

3.2. Kinetics analysis of exothermic reactions

Kinetics analysis of the exothermic reactions in sample An + Ele and sample Cat + An, is performed in this section based on the DSC tests at variant heating rates.

The DSC profile of sample An + Ele can be regarded as the superposition of the heat generation profiles of three exothermic reactions, i.e. the SEI film decomposition reaction, the reaction between anode active material and electrolyte, and the reaction between anode active material and binder, denoted as Q_{SEI}, $Q_{An\text{-}E}$ and $Q_{An\text{-}B}$, respectively, as illustrated in Fig. 4(a). Likewise, the heat generation of sample Cat + An is also divided into those from three reactions, denoted as $Q_{Cat\text{-}An}$, $Q_{Cat\text{-}B}$ and Q_{Cat}, representing the heat generation from the reaction between oxygen released from cathode active material and anode active material, the reaction between oxygen released from cathode active material and binder, and the decomposition of cathode active material, respectively, as shown in Fig. 4(b).

The basic kinetics equations of a chemical reaction are as follows:

$$\kappa_x = A_x \cdot \exp\left(-\frac{E_{a,x}}{RT}\right) \cdot f_x(c_x) \tag{1}$$

$$c_x = 1 - \int \kappa_x \, dt \tag{2}$$

κ_x is the reaction rate, c_x is the normalized concentration of the reactant x; A_x, $E_{a,x}$, and $f_x(c_x)$ are the kinetics triplets (pre-exponential factor, activation energy and mechanism function). The mechanism function $f_x(c_x)$ is commonly expressed as Eq. (3), where n_x is the reaction order. For an exothermic/endothermic reaction, the heat generation can be calculated by Eq. (4). m_x is the mass of the reactant and set as 9.4 mg for the DSC tests in this research, while ΔH_x is the reaction enthalpy.

$$f_x(c_x) = c_x^{n_x} \tag{3}$$

$$Q_x = m_x \cdot \Delta H_x \cdot \kappa_x \tag{4}$$

The kinetics parameters can be obtained by fitting the DSC profiles [35]. However, it is difficult to calculate all the kinetics parameters of multiple reactions in single DSC profile. In this paper, the Kissinger's method [38] is applied to pre-determine the pre-exponential factor A_x
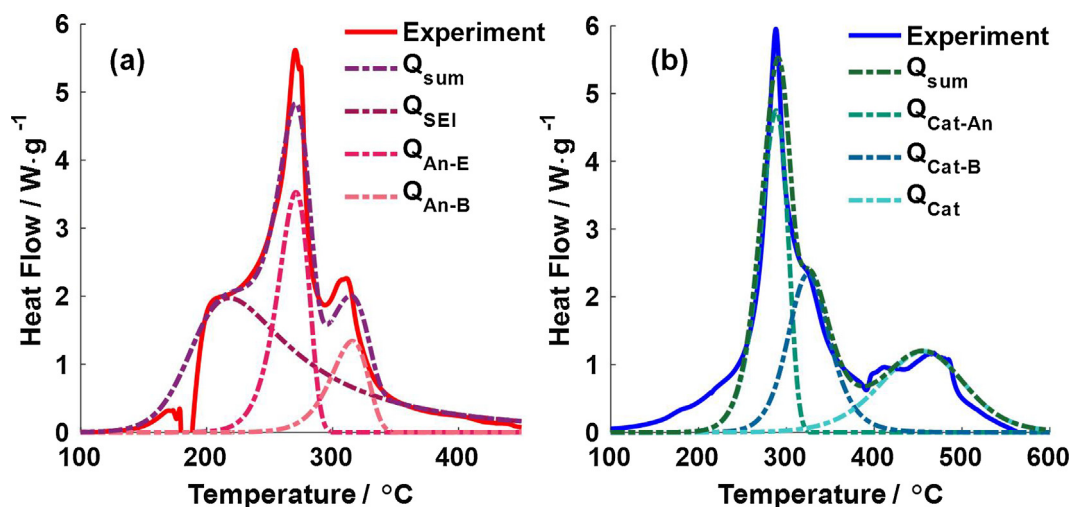

Fig. 4. Illustration of the exothermic reactions in (a) sample An + Ele and (b) sample Cat + An.
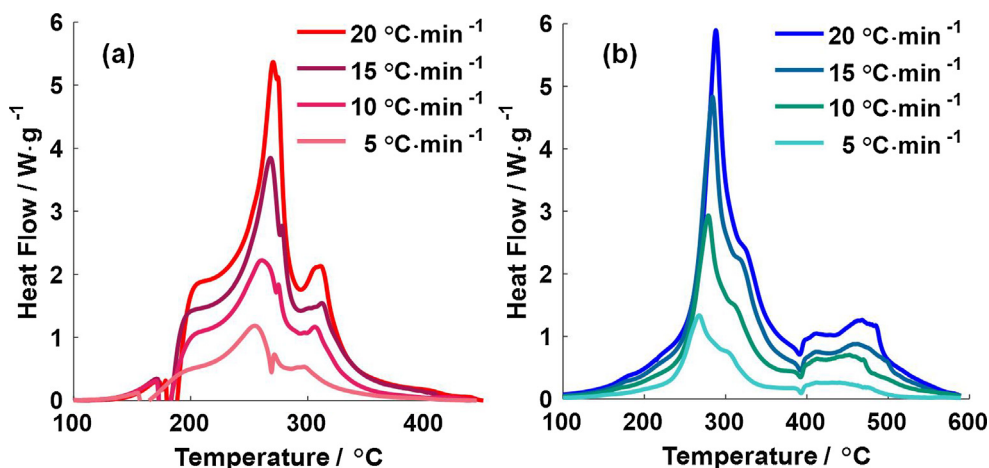
Fig. 5. DSC profiles at variant heating rates. (a) DSC profiles of sample An + Ele; (b) DSC profiles of sample Cat + An.

Table 4
Peak temperatures of the exothermic reactions.

Heating rate/°C min^{-1}	Sample An + Ele		Sample Cat + An	
	Peak$_{An-E}$/°C	Peak$_{An-B}$/°C	Peak$_{Cat-An}$/°C	Peak$_{Cat-B}$/°C
5	255.0	296.8	267.6	304.6
10	262.9	306.0	278.7	314.3
15	268.2	312.2	283.8	320.9
20	270.3	315.3	288.1	325.9

and activation energy $E_{a,x}$ of some exothermic reactions without considering the mechanism function.

For the DSC tests at variant heating rates, the variation of the peak temperature with heating rate follows the Kissinger's equation [38]:

$$\ln\left(\frac{\beta_i}{T_{p,i}^2}\right) = \ln\left(\frac{A_x R}{E_{a,x}}\right) - \frac{E_{a,x}}{RT_{p,i}}, \quad (i = 1, 2, 3, ..., u) \tag{5}$$

where β_i is the heating rate, $T_{p,i}$ is the peak temperature, and u is the number of variant heating rates. Then, the activation energy $E_{a,x}$ of can be derived from the slope of the $\ln\left(\frac{\beta}{T_p^2}\right) - \frac{1}{T_p}$ fitting straight line, while

the pre-exponential factor A_x can be obtained from the intercept on ordinate straight line.

Fig. 5(a) and (b) show the DSC profiles of sample An + Ele and sample Cat + An at variant heating rates, respectively. Table 4 shows the peak temperatures of four of the six exothermic reactions in sample An + Ele and sample Cat + An, while the peak temperatures of SEI film decomposition reaction and the cathode active material decomposition reaction are difficult to obtain from the DSC profiles accurately and are thus not listed in Table 4. The pre-exponential factors and activation energies of the two remaining reactions will be identified using non-linear fitting method later.

The variations of $\ln\left(\frac{\beta}{T_p^2}\right)$ as a function of $\frac{1}{T_p}$ are plotted in Fig. 6(a), where the symbols represent the tests data shown in Table 4 and the dash lines are the best fits of tests data using Eq. (5). The peak temperatures shifted to higher values as the heating rate increased, and good linear relationships between $\ln\left(\frac{\beta}{T_p^2}\right)$ and $\frac{1}{T_p}$ can be observed in Fig. 6(a). The pre-exponential factors and activation energies of the four exothermic reactions are then calculated according to Eq. (5). However, only limited kinetics parameters can be obtained using Kissinger's method, while the kinetics triplets of the two remaining reactions, the
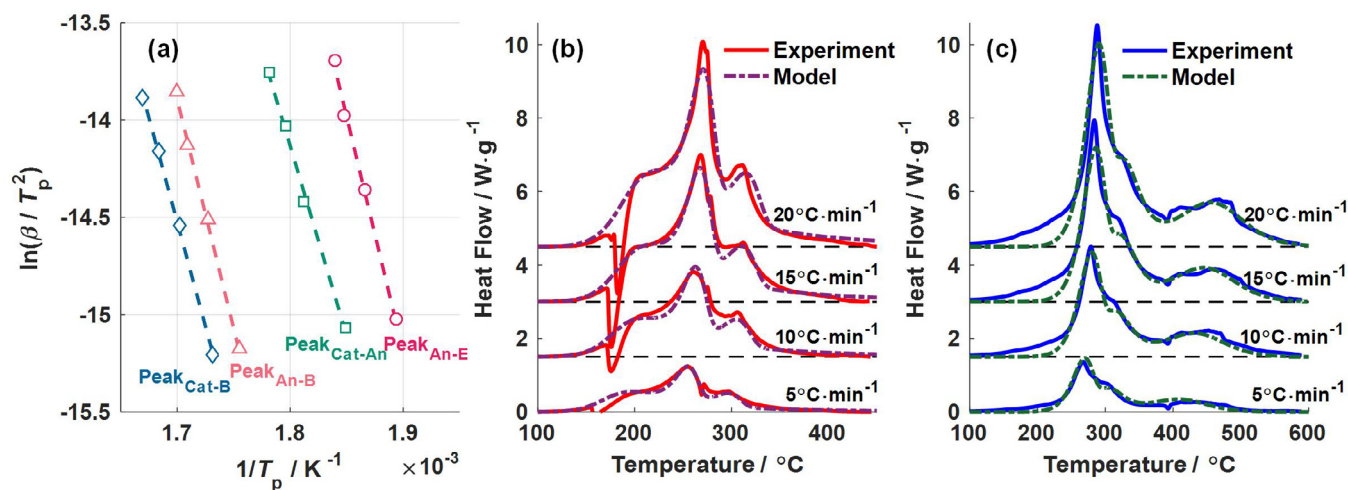

Fig. 6. Kinetics analysis of the exothermic reactions using Kissinger's method and nonlinear fitting method. (a) Calculation of kinetics parameters using Kissinger's method; (b) comparison of model predicted DSC profiles and experiment results of sample An + Ele; (c) comparison of model predicted DSC profiles and experiment results of sample Cat + An.

Table 5
Kinetics parameters of the exothermic reactions.

Sample	x	A_x/s^{-1}	$E_{\mathrm{a},x}/\mathrm{J\,mol}^{-1}$	n_x	$\Delta H_x/\mathrm{J\,g}^{-1}$
An + Ele	SEI	6.3623×10^9	1.0960×10^5	5.5	578.7
	An-E	5.1510×10^{17}	2.0077×10^5	1	253.2
	An-B	4.9679×10^{15}	1.9549×10^5	1	108.5
Cat + An	Cat-An	2.4262×10^{13}	1.6201×10^5	1	560.6
	Cat-B	6.5429×10^{13}	1.7785×10^5	2	452.1
	Cat	5.3481×10^5	1.0934×10^5	1.5	434.0

Table 6
Basic parameters of the 24 Ah batteries.

Parameter	Description	Unit	Value
M	Mass of the two batteries	g	1100
C_p	Specific heat capacity of the battery	$\mathrm{J\,g}^{-1}\mathrm{K}^{-1}$	1.1
A	Heat exchange area of the two batteries	m^2	0.0841
h	Heat exchange coefficient between the batteries and EV-ARC	$\mathrm{W\,K}^{-1}\mathrm{m}^{-2}$	7.5

reaction mechanism functions and the reaction enthalpies ΔH_x of all the six reactions remain unknown. Therefore, nonlinear fitting method is then applied to identify all the kinetics parameters of the six exothermic reactions.

For sample An + Ele, the heat generation is composed of those from three exothermic reactions and can be calculated by Eq. (6). Given a setting of the kinetics parameters $[A_x, E_{\mathrm{a},x}, n_x, \Delta H_x]$ of the three reactions, with some of them pre-determined using the Kissinger's method, the DSC profiles of sample An + Ele at variant heating rates can be simulated according to Eqs. (1)–(4) and (6). The root mean squared error (RMSE) between the model simulated DSC profiles and the experimental data is defined by Eq. (7) to evaluate the fitness of the model, where l_i is the total temperature points in the DSC profile at the heating rate of β_i and $T_{i,j}$ is the recorded temperature point. A smaller RMSE indicates a better degree of coincidence. Nonlinear fitting method, such as genetic algorithm, can be utilized to identify the kinetics parameters through minimizing the RMSE. Likewise, the kinetics parameters of the three exothermic reactions in sample Cat + An can also be characterized using nonlinear fitting method.

$$Q_{\mathrm{sum}} = Q_{\mathrm{SEI}} + Q_{\mathrm{An-E}} + Q_{\mathrm{An-B}} \tag{6}$$

$$\mathrm{RMSE} = \sqrt{\frac{\sum_{i=1}^{4}\sum_{j=1}^{l_i}(Q_{\mathrm{sum}}(T_{i,j})-Q_{\mathrm{exp}}(T_{i,j}))^2}{\sum_{i=1}^{4} l_i}} \tag{7}$$

A comparison of the model predicted DSC profiles and the experiment results of sample An + Ele and sample Cat + An at variant heating rates is presented in Fig. 6(b) and (c). The identified kinetics parameters are listed in Table 5. The predicted DSC profiles agree well with the experiment results at variant heating rates for both sample An + Ele and sample Cat + An, indicating that the identified kinetics parameters can describe the reaction mechanisms well and achieve good predictions of the heat generations of all the exothermic reactions.

3.3. Model-based TR predictions of lithium-ion batteries

A lumped model is established to predict the battery TR behaviors under thermal abuse conditions. The battery temperature can be calculated by Eqs. (8) and (9) according to the energy balance equation.

Table 7
Mass balance equations.

Reactant	Mass balance equation	
SEI film	$c_{\mathrm{SEI}} = 1 - \int \kappa_{\mathrm{SEI}}\mathrm{d}t$	(11)
Anode active material	$c_{\mathrm{An-E}} = c_{\mathrm{Cat-An}} = 1 - \int (\kappa_{\mathrm{An-E}} + \kappa_{\mathrm{Cat-An}})\mathrm{d}t$	(12)
Binder	$c_{\mathrm{An-B}} = c_{\mathrm{Cat-B}} = 1 - \int \left(\frac{\gamma}{1+\gamma}\cdot\kappa_{\mathrm{An-B}} + \kappa_{\mathrm{Cat-B}}\right)\mathrm{d}t$	(13)
Cathode active material	$c_{\mathrm{Cat}} = 1 - \int \kappa_{\mathrm{Cat}}\mathrm{d}t$	(14)

$M = 1100$ g is the mass of the two batteries and $C_p = 1.1\,\mathrm{J\,g}^{-1}\mathrm{K}^{-1}$ is the specific heat capacity measured using EV-ARC, as listed in Table 6. $T_{\mathrm{Bat},0}$ is the initial temperature of the two batteries. Q_{gen} and Q_{diss} are the total heat generation rate and the heat dissipation rate, respectively.

$$\frac{\mathrm{d}T_{\mathrm{Bat}}}{\mathrm{d}t} = \frac{Q_{\mathrm{gen}} + Q_{\mathrm{diss}}}{MC_p} \tag{8}$$

$$T_{\mathrm{Bat}}(t) = T_{\mathrm{Bat},0} + \int \frac{\mathrm{d}T_{\mathrm{Bat}}}{\mathrm{d}t}\mathrm{d}t \tag{9}$$

Q_{gen} is determined by the chemical reactions during the TR process. Besides the exothermic reactions characterized using DSC tests, the combustion of the organic solvents and the flammable gas (such as H_2, CO, CH_4, C_2H_6, and C_2H_4) would also occur and may contribute to Q_{gen}. However, the combustion always occurs outside the batteries and has little influence on battery temperature response, as the combustion energy is not fully utilized to heat the cell, but heat the surroundings [31,33,34]. Therefore, the contribution of combustion to the battery temperature response is neglected in the battery TR model. Q_{gen} can thus be regarded as the sum of the heat generation rates of all the six exothermic reactions, as in Eq. (10). The heat generation rates of the six exothermic reactions can be calculated by chemical kinetics equations (Eqs. (1)–(4)), with the kinetics parameters determined in Section 3.2. The mass of the reactant m_x is set as 608.4 g, 55.3% of the mass of the two batteries, according to the battery specification. However, the kinetics parameters of the six exothermic reactions are calculated from the DSC tests on sample An + Ele and sample Cat + An separately, while some of the exothermic reactions in the two samples consume the same reactants and interact with each other in the battery. Thus, the exothermic reactions should be coupled together according to the mass balance equations, as presented in Table 7, where $\gamma = 3.4/6$ is the mass ratio of binder in the anode and the cathode.

$$Q_{\mathrm{gen}} = Q_{\mathrm{SEI}} + Q_{\mathrm{An-E}} + Q_{\mathrm{An-B}} + Q_{\mathrm{Cat-An}} + Q_{\mathrm{Cat-B}} + Q_{\mathrm{Cat}} \tag{10}$$

Q_{diss} represents the heat exchange rate between the batteries and the EV-ARC and can be calculated by Eq. (15), where $A = 0.0841\,\mathrm{m}^2$ is the area of the batteries, and T_{ARC} is the temperature of the EV-ARC. $h = 7.5\,\mathrm{W\,K}^{-1}\mathrm{m}^{-2}$ is the heat exchange coefficient, a characteristic parameter of the EV-ARC system. h can be calculated according to the calibration test on an aluminum block with a similar size of the 24 Ah battery. An EV-ARC model is also built to simulate the change of T_{ARC} under different operating modes (Heat, Wait, Seek, Exotherm and Cool) according to the control strategy of the EV-ARC. Details of the EV-ARC model is presented in Fig. A1 (Appendix A).

$$Q_{\mathrm{diss}} = h \cdot A \cdot (T_{\mathrm{ARC}} - T_{\mathrm{Bat}}) \tag{15}$$

Model validation is carried out by comparing the model predictions with the TR tests results conducted in Section 2.2 using EV-ARC. Fig. 7 shows the model verification results under adiabatic TR test. The model predicted temperature vs. time profile and temperature rate vs. temperature profile both fit well with the adiabatic TR test result, as
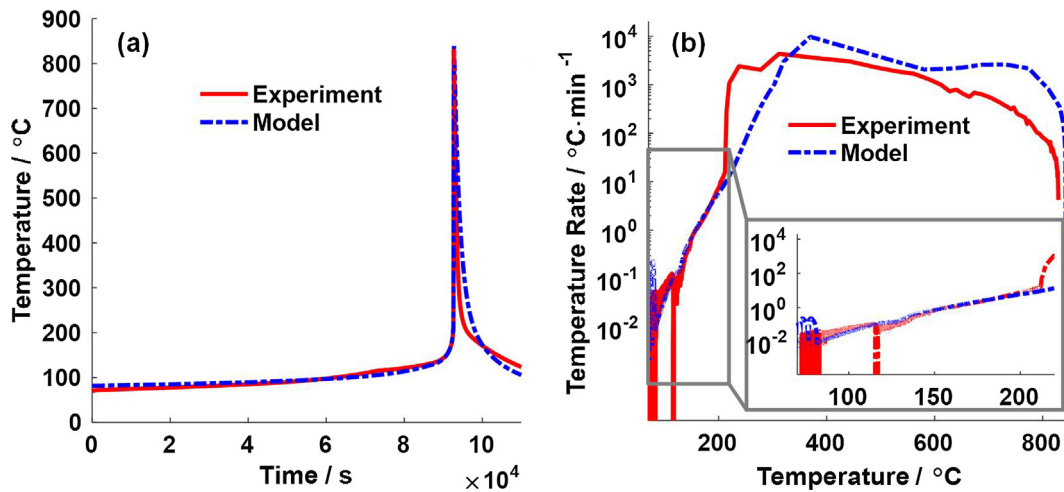
Fig. 7. Predictions of battery TR behaviors under adiabatic TR test. (a) The temperature vs. time profile; (b) the temperature rate vs. temperature profile.

Table 8
Comparison of the predicted and experimental critical temperatures under variant TR tests.

Tests	Experiment			Model		
	T_{onset}/°C	T_{TR}/°C	T_{max}/°C	T_{onset}/°C	T_{TR}/°C	T_{max}/°C
Adiabatic TR test	72.39	213.27	829.33	81.44	227.70	842.73
130 °C oven test	N/A	N/A	179.43	N/A	N/A	185.84
150 °C oven test	N/A	205.62	860.82	N/A	202.83	857.74

presented in Fig. 7(a) and (b).

Three critical temperatures, i.e. the onset temperature of self-heating, T_{onset}, which denotes the temperature when the self-heating rate of the batteries exceeds the defined exothermic rate threshold of 0.01 °C min⁻¹; the onset temperature of TR, T_{TR}, which is defined as the temperature when the battery temperature rate is higher than 20 °C min⁻¹; and the maximum temperature during the TR process, T_{max}, are applied to evaluate the battery safety performance in this research. The model predicted critical temperatures are compared with the experimental results in Table 8. The TR model can predict the T_{onset}
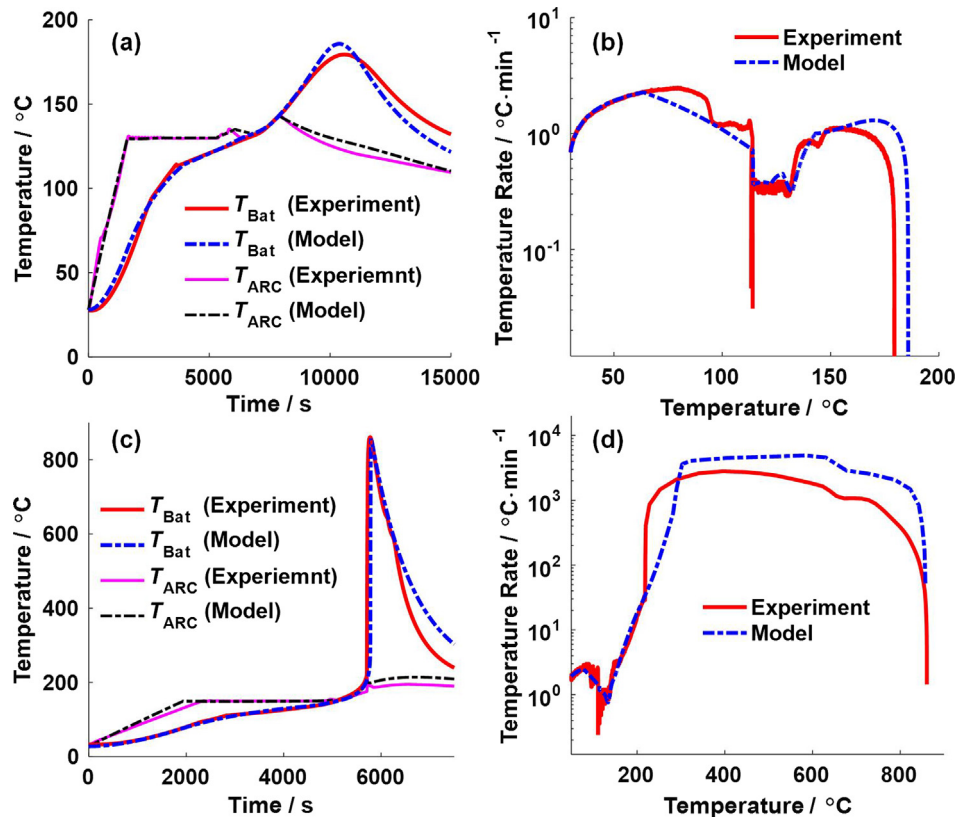

Fig. 8. Predictions of battery TR behaviors under oven tests. (a) and (b) Predictions of the 130 °C oven test; (c) and (d) predictions of the 150 °C oven test.

and T_{TR} under adiabatic condition accurately, as presented in Table 8. Furthermore, the predicted T_{max} reaches 842.73 °C, very close to the experimental result (829.33 °C), indicating that the reaction enthalpies derived from the DSC tests agree well with the total energy released during the TR process.

However, there are some deviations between model predictions and the experiment results. First, a decline of the battery temperature rate was observed in the experiment results at around 115 °C, resulting from the vaporization of the electrolyte and subsequent rupture of pouch bag [50,51], while the predicted temperature rate profile shows no decrease as the effects of electrolyte vaporization are not taken into consideration yet. The second deviation is that the experimental battery temperature rate increases to more than 2000 °C min^{-1} dramatically after TR happens, while the predicted temperature rate rises in a relative lower rate and reaches 2000 °C min^{-1} at around 300 °C. The sharp rise of experimental battery temperature rate is due to possible massive internal short circuit [55] and the violent reactions of all the cell components in a short time (as presented in Fig. 3(a)), which are difficult to simulate based on the investigations of cell components, and are thus not included in the TR model yet.

Despite those minor deviations in the temperature rate profile, the TR model based on the kinetics analysis of cell components can predict the battery adiabatic TR behaviors well, as the predicted temperature profile and the three critical temperatures are consistent with the experimental result, as shown in Fig. 7 and Table 8.

The TR model is further utilized to predict the battery safety behaviors under oven tests at variant temperatures, as presented in Fig. 8.

For the 130 °C oven test, the battery was gradually heated up to the oven temperature during the heat mode, and the EV-ARC went into wait mode for the battery to reach thermal equilibrium with the calorimeter, as shown in Fig. 8(a). The battery temperature went higher than the temperature of the EV-ARC in the middle-to-late stage of the wait mode, and continued to increase to around 180 °C after the EV-ARC was set to the cool mode. The model predicted battery temperature vs. time profile and temperature rate vs. temperature profile during 130 °C oven test both fit well with the experimental results, as presented in Fig. 8(a) and (b). The predicted T_{max} during the 130 °C oven test reaches 185.84 °C, consistent with the experimental result (179.43 °C).

For the 150 °C oven test, the battery ran into TR after heated to 150 °C and resting for 30 min, though the EV-ARC has been set to cool mode immediately. The maximum temperature T_{max} reached 857.74 °C during the 150 °C oven test. The TR model can also predict the battery TR behaviors under 150 °C oven test very well, for the predicted temperature vs. time profile and temperature rate vs. temperature profile both fit well with the experimental results, as shown in Fig. 8(c) and (d). The model predicted critical temperatures are also consistent with the experimental values, as presented in Table 8.

Overall, the TR model based on the kinetics analysis of cell components can quantitatively simulate the battery safety behaviors under both adiabatic test and oven test conditions, indicating that the model can achieve a good capture of the battery TR mechanism and can predict the exothermic behaviors of the battery accurately. Therefore, the TR model can be applied to determine the battery safety performance and optimize battery chemistry design only based on kinetics analysis of cell components, without producing test batches of batteries.

4. Conclusion

In this paper, a novel approach is proposed to predict the battery TR behaviors from kinetics analysis of cell components. The battery TR mechanism is investigated through DSC tests on the individual cell components and their mixtures. Six exothermic reactions are found to be the dominant heat sources during battery TR process. The battery heat generation is firstly attributed to the exothermic reactions on the anode/electrolyte interface, while the decomposition reactions of cathode active material and the reactions induced by the released oxygen begin after the temperature reaches around 250 °C.

Kinetics analysis is then performed on the six exothermic reactions, based on the DSC tests results at variant heating rates. Kissinger's method is firstly applied to pre-determine the pre-exponential factor A_x and activation energy $E_{a,x}$ of four reactions without considering the mechanism functions. Afterwards, nonlinear fitting method is utilized to identify all the kinetics parameters of the six exothermic reactions. The DSC profiles predicted by the kinetics models with the identified kinetics parameters agree well with the experiment results at variant heating rates, demonstrating that the kinetics models can achieve good predictions of the heat generations of the six exothermic reactions.

A predictive battery TR model is established by coupling the chemical kinetics models of the six exothermic reactions together. The model predictions can fit well with the adiabatic TR test results and the oven tests results for the 24 Ah lithium batteries, with the predicted temperature vs. time profile and temperature rate vs. temperature profile in good agreements with the experimental results. The model predicted critical temperatures (T_{onset}, T_{TR} and T_{max}) are also consistent with experiments results under variant TR tests. Hence, the TR model can be applied to determine the battery safety performance based on kinetics analysis of cell components, without producing test batches of batteries.

Our future work will focus on: (1) study the vaporization of the electrolyte and its effects on battery TR behaviors; (2) establish models for massive internal short circuit and those violent reactions when TR happens, to make our TR model more accurate.

Appendix A. The EV-ARC model

Fig. A1 presents the EV-ARC model for simulating the change of T_{ARC} under different operation modes. The parameters used in the EV-ARC model are listed in Table A1. As shown in Fig. A2, the model predicted T_{ARC} and T_{Bat} agree well with the experiment results except for minor difference in the onset temperature of self-heating.
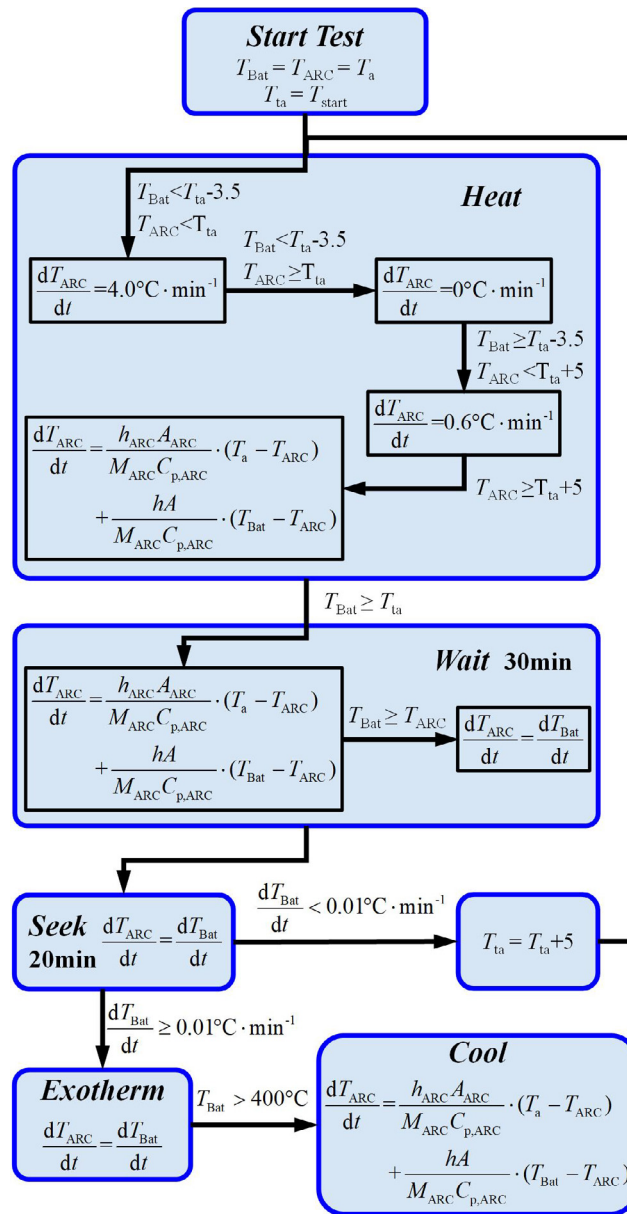
Start Test
$$T_{Bat} = T_{ARC} = T_a$$
$$T_{ta} = T_{start}$$

Heat

$T_{Bat} < T_{ta}-3.5$
$T_{ARC} < T_{ta}$

$$\frac{dT_{ARC}}{dt} = 4.0°C \cdot min^{-1}$$

$T_{Bat} < T_{ta}-3.5$
$T_{ARC} \geq T_{ta}$

$$\frac{dT_{ARC}}{dt} = 0°C \cdot min^{-1}$$

$T_{Bat} \geq T_{ta}-3.5$
$T_{ARC} < T_{ta}+5$

$$\frac{dT_{ARC}}{dt} = 0.6°C \cdot min^{-1}$$

$T_{ARC} \geq T_{ta}+5$

$$\frac{dT_{ARC}}{dt} = \frac{h_{ARC}A_{ARC}}{M_{ARC}C_{p,ARC}} \cdot (T_a - T_{ARC}) + \frac{hA}{M_{ARC}C_{p,ARC}} \cdot (T_{Bat} - T_{ARC})$$

$T_{Bat} \geq T_{ta}$

Wait **30min**

$$\frac{dT_{ARC}}{dt} = \frac{h_{ARC}A_{ARC}}{M_{ARC}C_{p,ARC}} \cdot (T_a - T_{ARC}) + \frac{hA}{M_{ARC}C_{p,ARC}} \cdot (T_{Bat} - T_{ARC})$$

$T_{Bat} \geq T_{ARC}$

$$\frac{dT_{ARC}}{dt} = \frac{dT_{Bat}}{dt}$$

Seek **20min** $\frac{dT_{ARC}}{dt} = \frac{dT_{Bat}}{dt}$

$\frac{dT_{Bat}}{dt} < 0.01°C \cdot min^{-1}$

$$T_{ta} = T_{ta}+5$$

$\frac{dT_{Bat}}{dt} \geq 0.01°C \cdot min^{-1}$

Exotherm
$$\frac{dT_{ARC}}{dt} = \frac{dT_{Bat}}{dt}$$

$T_{Bat} > 400°C$

Cool
$$\frac{dT_{ARC}}{dt} = \frac{h_{ARC}A_{ARC}}{M_{ARC}C_{p,ARC}} \cdot (T_a - T_{ARC}) + \frac{hA}{M_{ARC}C_{p,ARC}} \cdot (T_{Bat} - T_{ARC})$$

Fig. A1. The EV-ARC model based on the control strategy.

Table A1
The parameters used in the EV-ARC model.

| Symbol	Description	Value
T_{Bat}	The temperature of the tested battery	
T_{ARC}	The temperature of the EV-ARC	
T_a	Ambient temperature	25 °C
T_{ta}	Target temperature for the EV-ARC control system	
T_{start}	Start temperature of the TR tests	
h_{ARC}	The heat exchange coefficient between the EV-ARC and ambient	$3.2\,W\,K^{-1}\,m^{-2}$
A_{ARC}	The heat exchange area between the EV-ARC and ambient	$0.5483\,m^2$
M_{ARC}	The mass of the EV-ARC	15920 g
$C_{p,ARC}$	The heat capacity of the EV-ARC	$0.905\,J\,g^{-1}\,K^{-1}$
h	The heat exchange coefficient between the battery and the EV-ARC	$7.5\,W\,K^{-1}\,m^{-2}$
A	The heat exchange area between the battery and the EV-ARC	$0.0841\,m^2$
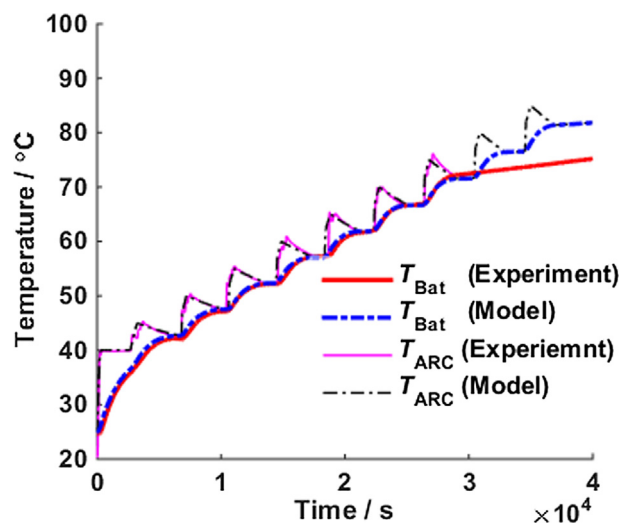
Fig. A2. Validation of the EV-ARC model.

Appendix B. Oxygen evolution of the cathode active material during heating

We have simultaneously monitored the heat generation and oxygen evolution of the cathode active material during heating (at $20\,^\circ\text{C min}^{-1}$) using the simultaneous thermogravimetry – differential scanning calorimetry (STA/TG-DSC) and mass spectroscopy (MS), as shown in Fig. B1. Oxygen evolution was observed when the cathode active material decomposes at elevated temperature, along with significant heat generation, due to the structural change of the cathode active material from layered to spinel, and then to rock-salt [23,25].
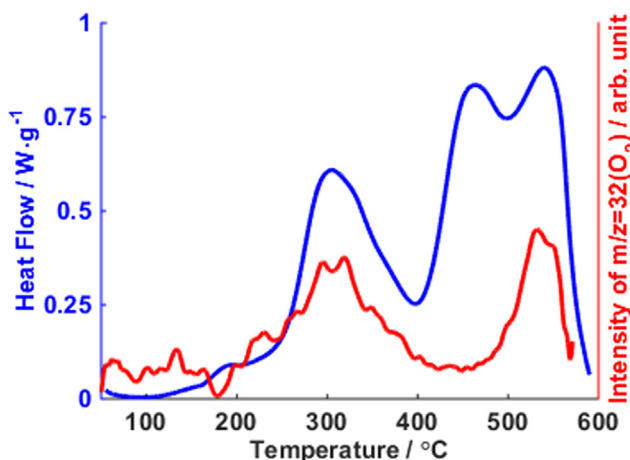

Fig. B1. Heat generation and oxygen evolution of the cathode active material during heating.

References

[1] Du J, Ouyang D. Progress of Chinese electric vehicles industrialization in 2015: a review. Appl Energy 2017;188:529–46. http://dx.doi.org/10.1016/j.apenergy.2016.11.129.

[2] Lu L, Han X, Li J, Hua J, Ouyang M. A review on the key issues for lithium-ion battery management in electric vehicles. J Power Sources 2013;226:272–88. http://dx.doi.org/10.1016/j.jpowsour.2012.10.060.

[3] Ding Y, Mu D, Wu B, Wang R, Zhao Z, Wu F. Recent progresses on nickel-rich layered oxide positive electrode materials used in lithium-ion batteries for electric vehicles. Appl Energy 2017;195:586–99. http://dx.doi.org/10.1016/j.apenergy.2017.03.074.

[4] Bresser D, Hosoi K, Howell D, Li H, Zeisel H, Amine K, et al. Perspectives of automotive battery R&D in China, Germany, Japan, and the USA. J Power Sources 2018;382:176–8. http://dx.doi.org/10.1016/j.jpowsour.2018.02.039.

[5] Ouyang M, Feng X, Han X, Lu L, Li Z, He X. A dynamic capacity degradation model and its applications considering varying load for a large format Li-ion battery. Appl Energy 2016;165:48–59. http://dx.doi.org/10.1016/j.apenergy.2015.12.063.

[6] Spotnitz R, Franklin J. Abuse behavior of high-power, lithium-ion cells. J Power Sources 2003;113:81–100. http://dx.doi.org/10.1016/S0378-7753(02)00488-3.

[7] Wang Q, Ping P, Zhao X, Chu G, Sun J, Chen C. Thermal runaway caused fire and explosion of lithium ion battery. J Power Sources 2012;208:210–24. http://dx.doi.org/10.1016/j.jpowsour.2012.02.038.

[8] Ye J, Chen H, Wang Q, Huang P, Sun J, Lo S. Thermal behavior and failure mechanism of lithium ion cells during overcharge under adiabatic conditions. Appl Energy 2016;182:464–74. http://dx.doi.org/10.1016/j.apenergy.2016.08.124.

[9] Feng X, Ouyang M, Liu X, Lu L, Xia Y, He X. Thermal runaway mechanism of lithium ion battery for electric vehicles: a review. Energy Storage Mater 2018;10:246–67. http://dx.doi.org/10.1016/j.ensm.2017.05.013.

[10] Chen Z, Xiong R, Lu J, Li X. Temperature rise prediction of lithium-ion battery suffering external short circuit for all-climate electric vehicles application. Appl Energy 2018;213:375–83. http://dx.doi.org/10.1016/j.apenergy.2018.01.068.

[11] Ruiz V, Pfrang A, Kriston A, Omar N, Van den Bossche P, Boon-Brett L. A review of international abuse testing standards and regulations for lithium ion batteries in electric and hybrid electric vehicles. Renew Sustain Energy Rev 2018;81:1427–52. http://dx.doi.org/10.1016/j.rser.2017.05.195.

[12] Belharouak I, Lu W, Vissers D, Amine K. Safety characteristics of Li $(Ni_{0.8}Co_{0.15}Al_{0.05})O_2$ and $Li(Ni_{1/3}Co_{1/3}Mn_{1/3})O_2$. Electrochem Commun 2006;8:329–35. http://dx.doi.org/10.1016/j.elecom.2005.12.007.

[13] Feng X, Fang M, He X, Ouyang M, Lu L, Wang H, et al. Thermal runaway features of large format prismatic lithium ion battery using extended volume accelerating rate calorimetry. J Power Sources 2014;255:294–301. http://dx.doi.org/10.1016/j.jpowsour.2014.01.005.

[14] Feng X, Sun J, Ouyang M, He X, Lu L, Han X, et al. Characterization of large format lithium ion battery exposed to extremely high temperature. J Power Sources 2014;272:457–67. http://dx.doi.org/10.1016/j.jpowsour.2014.08.094.

[15] Wang Q, Sun J, Yao X, Chen C. Thermal behavior of lithiated graphite with electrolyte in lithium-ion batteries. J Electrochem Soc 2006;153:A329–33. http://dx.doi.org/10.1149/1.2139955.

[16] Richard MN, Dahn JR. Accelerating rate calorimetry study on the thermal stability of lithium intercalated graphite in electrolyte. I. Experimental. J Electrochem Soc 1999;146:2068–77. http://dx.doi.org/10.1149/1.1391894.

[17] Richard MN, Dahn JR. Accelerating rate calorimetry study on the thermal stability of lithium intercalated graphite in electrolyte. II. Modeling the results and predicting differential scanning calorimeter curves. J Electrochem Soc 1999;146:2078–84. http://dx.doi.org/10.1149/1.1391894.

[18] Yang H, Bang H, Amine K, Prakash J. Investigations of the exothermic reactions of natural graphite anode for li-ion batteries during thermal runaway. J Electrochem Soc 2005;152:A73–9. http://dx.doi.org/10.1149/1.1836126.

[19] Chen Z, Qin Y, Ren Y, Lu W, Orendorff C, Roth EP, et al. Multi-scale study of thermal stability of lithiated graphite. Energy Environ Sci 2011;4:4023–30. http://dx.doi.org/10.1039/c1ee01786a.

[20] Forestier C, Grugeon S, Davoisne C, Lecocq A, Marlair G, Armand M, et al. Graphite electrode thermal behavior and solid electrolyte interphase investigations: role of state-of-the-art binders, carbonate additives and lithium bis(fluorosulfonyl)imide salt. J Power Sources 2016;330:186–94. http://dx.doi.org/10.1016/j.jpowsour.2016.09.005.

[21] Yamaki JI, Takatsuji H, Kawamura T, Egashira M. Thermal stability of graphite anode with electrolyte in lithium-ion cells. Solid State Ionics 2002;148:241–5. http://dx.doi.org/10.1016/S0167-2738(02)00060-7.

[22] Belharouak I, Vissers D, Amine K. Thermal stability of the $Li(Ni_{0.8}Co_{0.15}Al_{0.05})O_2$ cathode in the presence of cell components. J Electrochem Soc 2006;153:A2030–5. http://dx.doi.org/10.1149/1.2336994.

[23] Bak S, Hu E, Zhou Y, Yu X, Senanayake SD, Cho S, et al. Structural changes and thermal stability of charged $LiNi_xMn_yCo_zO_2$ cathode materials studied by combined in situ time-resolved XRD and mass spectroscopy. ACS Appl Mater Interf 2014;6:22594–601. http://dx.doi.org/10.1021/am506712c.

[24] Yamaki J, Shinjo Y, Doi T, Okada S. The rate equation for oxygen evolution by decomposition of LixCoO2 at elevated temperatures. J Electrochem Soc 2014;161:A1648–54. http://dx.doi.org/10.1149/2.0621410jes.

[25] Li J, Zhang Z, Guo X, Yang Y. The studies on structural and thermal properties of delithiated $Li_xNi_{1/3}Co_{1/3}Mn_{1/3}O_2$ ($0 < x \leq 1$) as a cathode material in lithium ion batteries. Solid State Ionics 2006;177:1509–16. http://dx.doi.org/10.1016/j.ssi.2006.03.055.

[26] Ping P, Wang Q, Huang P, Sun J, Chen C. Thermal behaviour analysis of lithium-ion battery at elevated temperature using deconvolution method. Appl Energy 2014;129:261–73. http://dx.doi.org/10.1016/j.apenergy.2014.04.092.

[27] Huang Q, Ma L, Liu A, Ma X, Li J, Wang J, et al. The reactivity of charged positive $Li_{1-n}[Ni_xMn_yCo_z]O_2$ electrodes with electrolyte at elevated temperatures using accelerating rate calorimetry. J Power Sources 2018;390:78–86. http://dx.doi.org/10.1016/j.jpowsour.2018.04.036.

[28] Inoue T, Mukai K. Roles of positive or negative electrodes in the thermal runaway of lithium-ion batteries: accelerating rate calorimetry analyses with an all-inclusive microcell. Electrochem Commun 2017;77:28–31. http://dx.doi.org/10.1016/j.elecom.2017.02.008.

[29] Inoue T, Mukai K. Are all-solid-state lithium-ion batteries really safe? − Verification by differential scanning calorimetry with an all-inclusive microcell. ACS Appl Mater Interf 2017;9:1507–15. http://dx.doi.org/10.1021/acsami.6b13224.

[30] Huang P, Wang Q, Li K, Ping P, Sun J. The combustion behavior of large scale lithium titanate battery. Sci Rep 2015;1–12. http://dx.doi.org/10.1038/srep07788.

[31] Huang P, Ping P, Li K, Chen H, Wang Q, Wen J, et al. Experimental and modeling analysis of thermal runaway propagation over the large format energy storage battery module with $Li_4Ti_5O_{12}$ anode. Appl Energy 2016;183:659–73. http://dx.doi.org/10.1016/j.apenergy.2016.08.160.

[32] Ribière P, Grugeon S, Morcrette M, Boyanov S, Laruelle S, Marlair G. Investigation on the fire-induced hazards of Li-ion battery cells by fire calorimetry. Energy Environ Sci 2012;5:5271–80. http://dx.doi.org/10.1039/C1EE02218K.

[33] Feng X, Sun J, Ouyang M, Wang F, He X, Lu L, et al. Characterization of penetration induced thermal runaway propagation process within a large format lithium ion battery module. J Power Sources 2015;275:261–73. http://dx.doi.org/10.1016/j.jpowsour.2014.11.017.

[34] Larsson F, Bertilsson S, Furlani M, Albinsson I, Mellander B-E. Gas explosions and thermal runaways during external heating abuse of commercial lithium-ion graphite-LiCoO2 cells at different levels of ageing. J Power Sources 2018;373:220–31. http://dx.doi.org/10.1016/j.jpowsour.2017.10.085.

[35] MacNeil DD, Dahn JR. Test of reaction kinetics using both differential scanning and accelerating rate calorimetries as applied to the reaction of Li_xCoO_2 in non-aqueous electrolyte. J Phys Chem A 2001;105:4430–9. http://dx.doi.org/10.1021/jp001187j.

[36] MacNeil DD, Dahn JR. The reactions of $Li_{0.5}CoO_2$ with nonaqueous solvents at elevated temperatures. J Electrochem Soc 2002;149:A912–9. http://dx.doi.org/10.1149/1.1483865.

[37] MacNeil DD, Christensen L, Landucci J, Paulsen JM, Dahn JR. An autocatalytic mechanism for the reaction of Li_xCoO_2 in electrolyte at elevated temperature. J Electrochem Soc 2000;147:970–9. http://dx.doi.org/10.1149/1.1393299.

[38] Kissinger HE. Variation of peak temperature with heating rate in differential thermal analysis. J Res Natl Bur Stand 1934;1956(57):217–21.

[39] Furushima Y, Yanagisawa C, Nakagawa T, Aoki Y, Muraki N. Thermal stability and kinetics of delithiated $LiCoO_2$. J Power Sources 2011;196:2260–3. http://dx.doi.org/10.1016/j.jpowsour.2010.09.076.

[40] Wang H, Tang A, Huang K. Oxygen evolution in overcharge $Li_xNi_{1/3}Co_{1/3}Mn_{1/3}O_2$ electrode and its thermal analysis kinetics. Chinese J Chem 2011;29:1583–8.

[41] Geder J, Hoster HE, Jossen A, Garche J, Yu DYW. Impact of active material surface area on thermal stability of $LiCoO_2$ cathode. J Power Sources 2014;257:286–92. http://dx.doi.org/10.1016/j.jpowsour.2014.01.116.

[42] Chen Z, Qin Y, Liu J, Amine K. Lithium difluoro(oxalato)borate as additive to improve the thermal stability of lithiated graphite. Electrochem Solid-State Lett 2009;12:A69–72. http://dx.doi.org/10.1149/1.3070581.

[43] Wang Q, Ping P, Sun J, Chen C. The effect of mass ratio of electrolyte and electrodes on the thermal stabilities of electrodes used in lithium ion battery. Thermochim Acta 2011;517:16–23. http://dx.doi.org/10.1016/j.tca.2011.01.015.

[44] Hatchard TD, MacNeil DD, Basu A, Dahn JR. Thermal model of cylindrical and prismatic lithium-ion cells. J Electrochem Soc 2001;148:A755–61. http://dx.doi.org/10.1149/1.1377592.

[45] Kim G-H, Pesaran A, Spotnitz R. A three-dimensional thermal abuse model for lithium-ion cells. J Power Sources 2007;170:476–89. http://dx.doi.org/10.1016/j.jpowsour.2007.04.018.

[46] Coman PT, Darcy EC, Veje CT, White RE. Numerical analysis of heat propagation in a battery pack using a novel technology for triggering thermal runaway. Appl Energy 2017;203:189–200. http://dx.doi.org/10.1016/j.apenergy.2017.06.033.

[47] Ping P, Wang Q, Chung Y, Wen J. Modelling electro-thermal response of lithium-ion batteries from normal to abuse conditions. Appl Energy 2017;205:1327–44. http://dx.doi.org/10.1016/j.apenergy.2017.08.073.

[48] Lopez CF, Jeevarajan JA, Mukherjee PP. Characterization of lithium-ion battery thermal abuse behavior using experimental and computational analysis. J Electrochem Soc 2015;162:A2163–73. http://dx.doi.org/10.1149/2.0751510jes.

[49] Peng P, Jiang F. Thermal behavior analyses of stacked prismatic $LiCoO_2$ lithium-ion batteries during oven tests. Int J Heat Mass Transf 2015;88:411–23. http://dx.doi.org/10.1016/j.ijheatmasstransfer.2015.04.101.

[50] Coman PT, Veje CT, White RE. Modeling vaporization, gas generation and venting in li-ion battery cells with a dimethyl carbonate electrolyte. J Electrochem Soc 2017;164:A1858–65. http://dx.doi.org/10.1149/2.0631709jes.

[51] Coman PT, Rayman S, White RE. A lumped model of venting during thermal runaway in a cylindrical Lithium Cobalt Oxide lithium-ion cell. J Power Sources 2016;307:56–62. http://dx.doi.org/10.1016/j.jpowsour.2015.12.088.

[52] Zhao R, Liu J, Gu J. Simulation and experimental study on lithium ion battery short circuit. Appl Energy 2016;173:29–39. http://dx.doi.org/10.1016/j.apenergy.2016.04.016.

[53] Feng X, Weng C, Ouyang M, Sun J. Online internal short circuit detection for a large format lithium ion battery. Appl Energy 2016;161:168–80. http://dx.doi.org/10.1016/j.apenergy.2015.10.019.

[54] Xu J, Liu B, Wang X, Hu D. Computational model of 18650 lithium-ion battery with coupled strain rate and SOC dependencies. Appl Energy 2016;172:180–9. http://dx.doi.org/10.1016/j.apenergy.2016.03.108.

[55] Feng X, He X, Ouyang M, Lu L, Wu P, Kulp C, et al. Thermal runaway propagation model for designing a safer battery pack with 25 Ah $LiNi_xCo_yMn_zO_2$ large format lithium ion battery. Appl Energy 2015;154:74–91. http://dx.doi.org/10.1016/j.apenergy.2015.04.118.

[56] Liu B, Yin S, Xu J. Integrated computation model of lithium-ion battery subject to nail penetration. Appl Energy 2016;183:278–89. http://dx.doi.org/10.1016/j.apenergy.2016.08.101.

[57] Ren D, Feng X, Lu L, Ouyang M, Zheng S, Li J, et al. An electrochemical-thermal coupled overcharge-to-thermal-runaway model for lithium ion battery. J Power Sources 2017;364:328–40. http://dx.doi.org/10.1016/j.jpowsour.2017.08.035.

[58] Eshetu GG, Grugeon S, Laruelle S, Boyanov S, Lecocq A, Bertrand J-P, et al. In-depth safety-focused analysis of solvents used in electrolytes for large scale lithium ion batteries. Phys Chem Chem Phys 2013;15:9145–55. http://dx.doi.org/10.1039/c3cp51315g.

[59] Markevich E, Salitra G, Aurbach D. Influence of the PVdF binder on the stability of $LiCoO_2$ electrodes. Electrochem Commun 2005;7:1298–304. http://dx.doi.org/10.1016/j.elecom.2005.09.010.